

Differentiated Backprojection Domain Deep Learning for Conebeam Artifact Removal

Yoseob Han, Junyoung Kim, and Jong Chul Ye, *Senior Member, IEEE*

Abstract—Conebeam CT using a circular trajectory is quite often used for various applications due to its relative simple geometry. For conebeam geometry, Feldkamp, Davis and Kress algorithm is regarded as the standard reconstruction method, but this algorithm suffers from so-called conebeam artifacts as the cone angle increases. Various model-based iterative reconstruction methods have been developed to reduce the cone-beam artifacts, but these algorithms usually require multiple applications of computational expensive forward and backprojections. In this paper, we develop a novel deep learning approach for accurate conebeam artifact removal. In particular, our deep network, designed on the differentiated backprojection domain, performs a data-driven inversion of an ill-posed deconvolution problem associated with the Hilbert transform. The reconstruction results along the coronal and sagittal directions are then combined using a spectral blending technique to minimize the spectral leakage. Experimental results show that our method outperforms the existing iterative methods despite significantly reduced runtime complexity.

Index Terms—Computed Tomography, Cone-beam artifact, Deep Learning, Spectral blending

I. INTRODUCTION

Conebeam X-ray CT with a large number of detector rows is often used for interventional imaging, dental CT, etc, due to the capability of obtaining high-resolution projection images with a relative simple scanner geometry. For the conebeam geometry, Feldkamp, Davis and Kress (FDK) algorithm [1] has been extensively used as a standard reconstruction method. Unfortunately, the FDK algorithm for conebeam CT usually suffers from conebeam artifacts. To address this problem, some researchers have proposed modified FDK algorithms by introducing angle-dependent weighting on the measured projection, [2]–[4]. However, these methods usually work for small cone angles.

Mathematically, conebeam artifacts arise from inherent defects in the circular trajectory that does not satisfy the Tuy’s condition [5]. In Fourier domain, this is manifested as the missing spectral components at the specific frequencies that are determined by the scanner geometry [6]–[8]. Accordingly, without the use of additional prior information, accurate removal of the conebeam artifacts may not be feasible.

To address this issue, several model-based iterative reconstruction (MBIR) methods [9]–[12] have been proposed by imposing total variation (TV) and other penalties. The role of

the penalty function is to impose the constrain to compensate for the missing frequency. Unfortunately, these algorithms are computationally expensive due to the iterative applications of 3-D projection and backprojection.

In recent years, deep learning approaches have been successfully used for a variety of applications [13]–[22] from image classification to medical image reconstruction. In X-ray CT, various deep learning reconstruction methods have been developed for low-dose CT [16], [17], [19], sparse-view CT [15], [18], [20], interior tomography [21], [22], and so on. These deep learning approaches usually outperform MBIR methods in their image quality and reconstruction time. In addition, in recent theoretical works [23], [24], the authors showed that a deep convolutional neural network with an encoder-decoder structure is related to a novel frame expansion using combinatorial convolutional frames. More specifically, thanks to the rectified linear unit (ReLU) nonlinearities, the input space is partitioned into large number of non-overlapping regions so that input images for each region share the same linear frame representation [24]. Therefore, once a neural network is trained, each input image can automatically choose the appropriate linear representation.

Inspired by these findings, here we propose a deep neural network for conebeam artifact removal. Instead of using standard image domain implementation of deep neural networks, we are aiming for a further step. Specifically, we have shown in our prior work [25] that the conebeam reconstruction problem can be solved by successive 2-D reconstruction in the differentiated backprojection (DBP) domain and subsequent spectral mixing to minimize spectral loss. This was due to the exact factorization of the initial 3-D conebeam reconstruction problem into a set of independent 2-D inversion problems as proposed by [26]. Furthermore, in our recent paper [22] for interior tomography problem, we have also demonstrated that deep neural networks on the DBP domain generalize better than the image domain approaches [21]. By synergistically combining these findings, we propose a DBP domain deep learning framework for cone-beam artifact removal. Specifically, as shown in Fig. 1, the input of our neural networks is the DBP images either in the coronal and sagittal directions, and our deep neural network is trained to solve a deconvolution problem involving Hilbert transform. Finally, the reconstructed 3-D volumes along the coronal and sagittal directional DBP are blended into a one 3-D volume using spectral mixing techniques. Theoretical justifications for each step are provided to support the efficacy of the proposed method.

This paper is structured as follows. In Section II, the

Y. Han, J. Kim, and J. C. Ye are with the Department of Bio and Brain Engineering, Korea Advanced Institute of Science and Technology (KAIST), Daejeon 34141, Republic of Korea (e-mail: {hanyoseob, junyoung.kim, jong.ye}@kaist.ac.kr). J.C. Ye is also with the Department of Mathematical Sciences, KAIST.

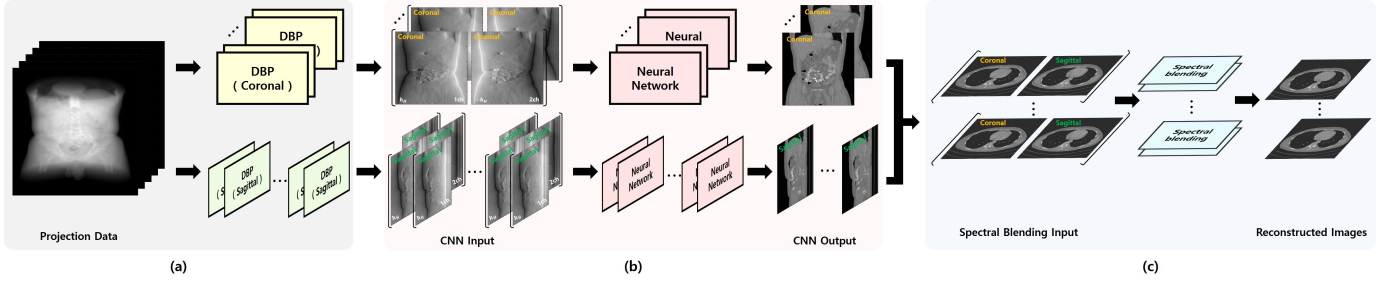


Fig. 1: Overview for differentiated backprojection domain deep learning. (a) shows the differentiated backprojection parts of coronal and sagittal directions, respectively. (b) illustrates the neural network part, and (c) shows the spectral blending.

mathematical preliminaries for conebeam CT using a circular trajectory are provided. Section III then discusses our main contributions: the DBP domain deep neural network and spectral blending. The experimental data set and the neural network training are explained in Section IV. The experimental results are given in Section V, which is followed by conclusions in Sections VI.

II. MATHEMATICAL PRELIMINARIES

A. Notation

Let $\mathbf{x} = (x, y, z)$ denote the point in \mathbb{R}^3 , where x, y and z are the Cartesian coordinates with respect to the patient. For the circular trajectory, the X-ray source rotates around the object $f(\mathbf{x})$ such that the source trajectory is represented by

$$\mathbf{a}(\lambda) = [R \cos \lambda \quad R \sin \lambda \quad 0]^\top, \quad \lambda \in [0, 2\pi], \quad (1)$$

where R denotes the radius of the circular scan. In this paper, the symbol $^\top$ denotes the transpose of a matrix or vector.

The X-ray transform D_f , which maps $f(\mathbf{x})$ into the set of its line integrals, is defined as

$$D_f(\mathbf{a}, \boldsymbol{\theta}) = \int_{-\infty}^{\infty} dt f(\mathbf{a} + t\boldsymbol{\theta}), \quad (2)$$

where $\boldsymbol{\theta}$ denote a vector on the unit sphere $\mathbb{S} \in \mathbb{R}^3$. The 3-D inverse Fourier transform is defined by

$$f(\mathbf{x}) = \frac{1}{(2\pi)^3} \int d\boldsymbol{\omega} \hat{f}(\boldsymbol{\omega}) e^{i\boldsymbol{\omega}^\top \mathbf{x}}, \quad (3)$$

where $\hat{f}(\boldsymbol{\omega})$ denotes the Fourier spectrum of $f(\mathbf{x})$, $\boldsymbol{\omega} \in \mathbb{R}^3$ refers to the angular frequency, and $i = \sqrt{-1}$.

B. Differentiated Backprojection (DBP)

For a given X-ray source trajectory $\mathbf{a}(\lambda)$, the differentiated backprojection (DBP) on a point $\mathbf{x} \in \mathbb{R}^3$ using the projection data from x-ray source trajectory $\mathbf{a}(\lambda)$, $\lambda \in [\lambda^-, \lambda^+]$ is defined as [27]–[29]:

$$g(\mathbf{x}) = \int_{\lambda^-}^{\lambda^+} d\lambda \frac{1}{\|\mathbf{x} - \mathbf{a}(\lambda)\|} \left. \frac{\partial}{\partial \mu} D_f(\mathbf{a}(\mu), \boldsymbol{\theta}) \right|_{\mu=\lambda}, \quad (4)$$

where $1/\|\mathbf{x} - \mathbf{a}(\lambda)\|$ is the magnification factor dependent weighting. One of the most fundamental properties of the DBP is its relationship to Fourier transform (3). Specifically, the DBP data in (4) can be represented as [25], [29]:

$$g(\mathbf{x}) = \frac{1}{(2\pi)^3} \int d\boldsymbol{\omega} \hat{f}(\boldsymbol{\omega}) e^{i\boldsymbol{\omega}^\top \mathbf{x}} \sigma(\mathbf{x}, \boldsymbol{\omega}, \lambda^\pm), \quad (5)$$

where

$$\sigma(\mathbf{x}, \boldsymbol{\omega}, \lambda^\pm) = i\pi [\text{sgn}(\boldsymbol{\omega}^\top \boldsymbol{\alpha}(\lambda^-, \mathbf{x})) - \text{sgn}(\boldsymbol{\omega}^\top \boldsymbol{\alpha}(\lambda^+, \mathbf{x}))], \quad (6)$$

and

$$\boldsymbol{\alpha}(\lambda, \mathbf{x}) = \frac{\mathbf{x} - \mathbf{a}(\lambda)}{\|\mathbf{x} - \mathbf{a}(\lambda)\|}. \quad (7)$$

Compared to the Fourier formulation in (3), the main difference of (5) is the additional term $\sigma(\mathbf{x}, \boldsymbol{\omega}, \lambda^\pm)$. This suggests that DBP provides a filtered version of $f(\mathbf{x})$. Since the spectrum of the filter $\sigma(\mathbf{x}, \boldsymbol{\omega}, \lambda^\pm)$ also depends on \mathbf{x} , the corresponding filter is a spatially varying filter.

C. Factorized Representation of Conebeam Geometry

For the conebeam CT with the circular trajectory, Dennerlein et al [26] proposed a factorization method. Similar idea was proposed by Yu et al [30], so we introduce the key ideas of these factorization methods.

Figure 2 illustrates the geometry of conebeam CT with circular trajectories. Here, consider a plane that is parallel to the z -axis and intersects the source trajectory at two locations $\mathbf{a}(\lambda^-)$ and $\mathbf{a}(\lambda^+)$. Let \mathcal{P} denote such a plane of interest. Then, the main goal of the factorization methods [26], [30] is to convert the 3-D reconstruction problem to a successive 2-D problems on the planes of interest. Specifically, on a plane of interest \mathcal{P} , we define virtual chord lines and virtual source locations. The virtual chord line coordinate system is defined by the virtual chord line direction \mathbf{e} , the z -axis \mathbf{e}_z , and their perpendicular axis \mathbf{e}^\perp . The virtual sources $\mathbf{a}_v(\lambda^+)$, $\mathbf{a}_v(\lambda^-)$ can be simply computed as

$$\mathbf{a}_v(\lambda) = \mathbf{a}(\lambda) + z\mathbf{e}_z.$$

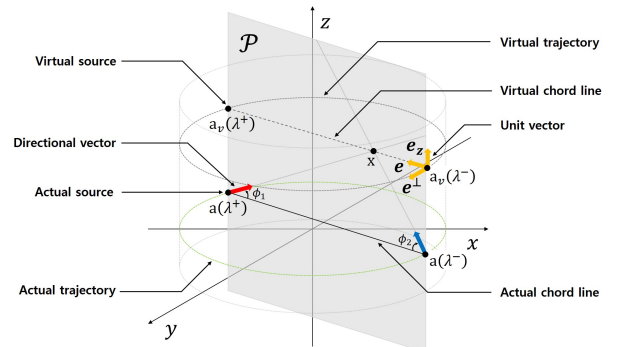


Fig. 2: Coordinate system on a factorized conebeam geometry.

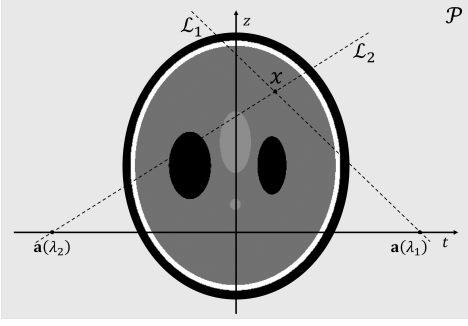


Fig. 3: Source geometry and filtering directions on the plane of interests.

Then, Cartesian coordinate \mathbf{x} is now converted to a new coordinate (t, s, z) such that

$$\mathbf{x} = t\mathbf{e} + s\mathbf{e}^\perp + z\mathbf{e}_z. \quad (8)$$

On a given plane of interest \mathcal{P} with a fixed s , with a slight abuse of notation, the object density and the DBP data can be represented by the following 2-D functions

$$f(t, z) := f(\mathbf{x}(t, z)), \quad g(t, z) := g(\mathbf{x}(t, z)).$$

Since the first and the second term in $\sigma(\mathbf{x}, \omega, \lambda^\pm)$ in (6) corresponds to the Hilbert transform along $\alpha(\lambda^-, \mathbf{x})$ and $\alpha(\lambda^+, \mathbf{x})$ direction, respectively, the authors in [26] showed that (5) can be simply represented as

$$g(t, z) = \pi \int_{-\infty}^{\infty} h_H(t - \tau) (f(\tau, z_1(\tau)) + f(\tau, z_2(\tau))) d\tau, \quad (9)$$

where $h_H(t)$ denotes the Hilbert transform, and $z_1(\tau)$ and $z_2(\tau)$ refer to the coordinate along \mathcal{L}_1 and \mathcal{L}_2 lines as shown in Fig. 3. This implies that the conebeam reconstruction problem can be solved by solving deconvolution problem in the DBP domain.

III. MAIN CONTRIBUTION

A. Encoder-Decoder CNNs for Deconvolution on \mathcal{P}

Although (9) suggests that a deconvolution algorithm can recover the original image $f(t, z)$ from $g(t, z)$ on each plane of interest \mathcal{P} , there are two technical difficulties. First, the grid for the unknown image is not a standard cartesian grid due to the t dependent $z_1(t)$ and $z_2(t)$ coordinates. In fact, $f(t, z_1(t))$ and $f(t, z_2(t))$ can be regarded as deformed images of $f(t, z)$ on new coordinate systems. Therefore, the convolution filter is spatially varying, so standard deconvolution methods do not work. Second, the deconvolution problem is highly ill-posed, since each DBP data $g(t, z)$ has contribution from two deformed images, $f(t, z_1(t))$ and $f(t, z_2(t))$. Accordingly, the authors in [26] proposed a regularized matrix inversion approach after the discretization of the intergration with respect to the original fixed cartesian grid for the unknown images.

In general, a deconvolution algorithm for (9) can be represented as a mapping:

$$\mathcal{T} : g \mapsto f, \quad g \in \mathcal{X}, f \in \mathcal{Y} \quad (10)$$

where \mathcal{X} denotes the input space where DBP data $g(t, z)$ lives, and \mathcal{Y} refers to the space that the image $f(t, z)$ belongs.

For the case of Tikhonov regularization, \mathcal{T} has a closed form expression; but for general regularization functions such as l_1 or total variation (TV), the inverse mapping \mathcal{T} is generally nonlinear, and should be found using computationally expensive iterative methods. A quick remedy to reduce the run-time computational complexity would be precalculating nonlinear mapping \mathcal{T} . Unfortunately, as the mapping \mathcal{T} depends on the input, storing \mathcal{T} for all inputs will require huge amount of memory and is not even feasible.

In this regard, an encoder-decoder CNNs (E-D CNN) using ReLU nonlinearities provides an ingenious way of addressing this issue. Specifically, in our recent theoretical work [24], which is also briefly summarized in Appendix for self-containment, we have shown that an encoder-decoder CNN with ReLU nonlinearity generates large number of locally linear mappings. More specifically, the input space \mathcal{X} is partitioned into non-overlapping regions where input for each region shares the common linear representation. Then, the switching to the corresponding linear representation for each input can be done instantaneously based on the ReLU activation patterns.

Another unique aspect of deep neural network is that these exponentially many linear representations can be derived from a small set of filter sets thanks to the combinatorial nature of the ReLU nonlinearities. Specifically, the network training is to estimate the filter set Θ :

$$\min_{\Theta} \sum_{i=1}^N \|f^{(i)} - \mathcal{T}_{\Theta} g^{(i)}\|_2^2, \quad (11)$$

where $\{(f^{(i)}, g^{(i)})\}_{i=1}^N$ denotes the training data set composed of ground-truth image and DBP image, and

$$\mathcal{T}_{\Theta} : g \mapsto f, \quad g \in \mathcal{X}, f \in \mathcal{Y}$$

refers to the inverse mapping parameterized by Θ . Usually, filter parameters Θ require much smaller memory and space. On the other hand, the number of associated linear representations increases exponentially with the network depth, width, and skipped connection.

This amazing expressivity and the input adaptability are believed to one of the main reasons for the success of deep neural network for image reconstruction problems.

B. Spectral Blending

Although the factorization method leads to 2-D deep learning approach for each plane of interest, Theorem 2.2 in our previous work [25] showed that the missing frequency region depends on the direction of the plane of interest. However, we also showed in our prior work [25] that at any point \mathbf{x} , if the missing frequency regions for different filtering directions are appropriately combined, we can minimize the artifacts from the missing frequency regions. This section describes this in detail.

Suppose that we are interested in recovering a voxel at $\mathbf{x} = (x, y, z)$ from the DBP data. Figure 4(a) illustrates the top view of a point \mathbf{x} and a source trajectory. In Figure 4(a), $\mathbf{a}_v(\lambda)$ denotes the corresponding virtual source location.

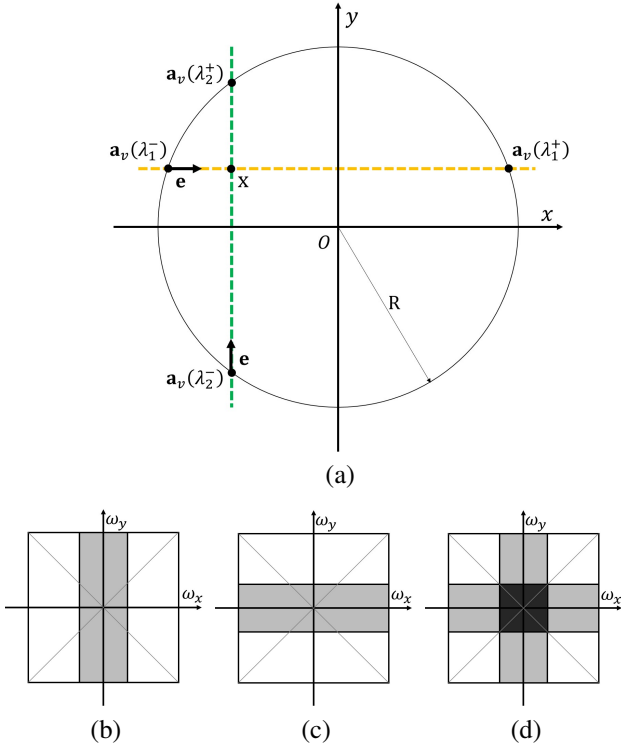


Fig. 4: The missing frequency region. (a) The top view of a point $\mathbf{x} = (x, y, z)$ and an source trajectory. The yellow line indicates the coronal directional plane of interest, and the green line denotes the sagittal directional plane of interest. (b)(c) The missing frequency region for coronal and sagittal directional processing, respectively. (d) The dark region denotes a common missing frequency region, respectively.

Now, consider the image reconstruction along the coronal direction where the plane of interest \mathcal{P} is aligned in the horizontal direction (for example, between $\mathbf{a}_v(\lambda_1^-)$ and $\mathbf{a}_v(\lambda_1^+)$). According to the spectral analysis in [25], the resulting DBP data has missing frequency regions along sagittal direction as illustrated in Figure 4(b). Therefore, any deconvolution algorithm using the coronal directional DBP data may have noise boosting along the sagittal direction due to the ill-posedness in the missing frequency regions. Similarly, for the DBP data along sagittal direction (for example, between $\mathbf{a}_v(\lambda_2^-)$ and $\mathbf{a}_v(\lambda_2^+)$), the corresponding missing frequency region is given by Figure 4(c), which results in the noise-boosting after the deconvolution. This leads to an important question: which directional plane we should choose?

For the case of full scan conebeam CT, there are redundancy in the 2-D factorization of the 3-D data, which can be exploited to answer the question. More specifically, we can perform reconstruction for both coronal and sagittal directions, and combine them. Figure 4(d) is the resulting missing frequency regions by combining the reconstruction results from two directions. In particular, the common missing frequency region is a dark square centered at the origin, which is the intersection of the two missing frequency regions in coronal and sagittal processing. This implies that except for the common frequency

regions, the missing spectral components in coronal directional processing can be compensated by the results from the sagittal processing, and vice versa.

Fig. 5 shows a flowchart for the spectral blending that was proposed in [25] to achieve this synergistic combination. In particular, the axial images f^{cor} and f^{sag} from coronal and sagittal reconstructed 3-D volumes are first converted to the spectral domain using the 2-D Fourier transform. Due to the ill-posedness along the missing frequency regions, streak pattern artifacts, as indicated by the yellow arrows in Fig. 5(b), are usually visible in the Fourier domain along the missing frequency region. Then, we apply the bow-type spectral weighting to suppress the signal in the missing frequency regions and combined them together. This process can be mathematically represented by

$$f^{com} = \mathcal{F}^{-1} \{w \odot \mathcal{F}\{f^{cor}\} + (1 - w) \odot \mathcal{F}\{f^{sag}\}\}.$$

where \mathcal{F} and \mathcal{F}^{-1} denote the Fourier and inverse Fourier transforms, respectively; w is the bow-tie spectral mask, and \odot denotes the element-wise multiplication.

IV. METHOD

A. Data set

Ten subject data sets from American Association of Physicists in Medicine (AAPM) Low-Dose CT Grand Challenge were used in this study. From the volume image data, conebeam CT sinogram data are numerically obtained using forward cone-beam projection. The number of detectors is 1440×1440 elements with pitch of 1 mm^2 . The number of views is 1200. The distance from source to origin (DSO) is 500 mm, and the distance from source to detector (DSD) is 1000 mm. The maximum cone angle is calculated as 35.8° . The $x - y$ size of images is 512×512 and the z size ranges from 400 to 600, but varies from the patient to the patient. Out of ten patient, eight patient data were used as training sets, one patient data was used as validation set, and the other patient data was used for test set. Since our neural network is trained on the plane of interest along the coronal and sagittal slices, the training dataset also consists of coronal and sagittal slices. This corresponds to $8192 (512 \times 8 \times 2)$, $1024 (512 \times 1 \times 2)$ coronal/sagittal slices for training and validation, respectively.

To investigate the network performance in a more quantitative way, we also conducted the experiments using numerical phantoms. Fig 6 shows a typical example of numerical phantom composed of disks with the same thickness and the spacing between the adjacent disks. The radius of disk is 80 mm. By changing the size, radius, the number, thickness, and spacing as shown in Table I, we created various phantoms.

	(a)	(b)	(c)	(d)
Thickness [mm]	10	14	20	16
Spacing [mm]	10	14	20	16
# of disks	9	7	5	7

TABLE I: Specification of disk phantom parameters. (a)(b)(c) were used for fine-tuning, and (d) was used for test.

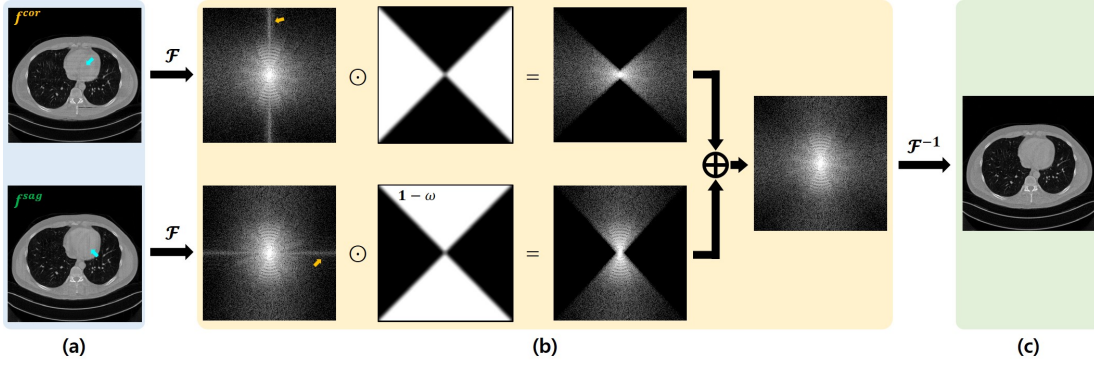


Fig. 5: Flowchart for the spectral blending. (a) shows axial images from the coronal and sagittal directional processed 3-D reconstruction by neural networks. (b) illustrates spectral blending, and (c) shows reconstruction result from spectral blending.

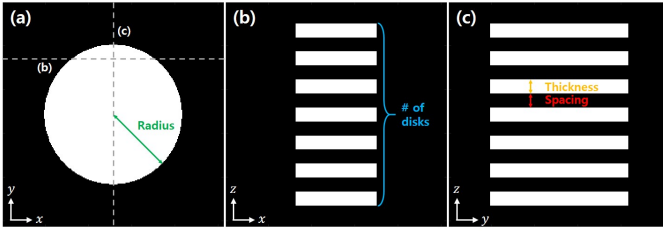


Fig. 6: Disk phantom. (a) shows the disk image on the axial plane. (b) and (c) illustrates cut-views from coronal and sagittal planes, respectively.

B. Algorithm Implementation

Fig. 7 illustrates the input and output of the proposed deep learning methods. Both coronal and sagittal view DBP images are used as inputs, and the artifact-free coronal and sagittal view images are used as labels. For the full scan conebeam CT, the DBP images on the plane of interest \mathcal{P} can be obtained using the two complementary source trajectories, i.e. $\mathbf{a}(\lambda)$ for $\lambda \in [\lambda^-, \lambda^+]$ and $\lambda \in [0, 2\pi] \setminus [\lambda^-, \lambda^+]$, respectively, where \setminus denotes the set complement, i.e. $A \setminus B = A \cap B^c$. In this case, we use both DBP images as inputs as shown in Fig. 7.

The network backbone corresponds to a modified architecture of U-Net [14] as shown in Fig. 8. A yellow arrow in Fig. 8 is the basic operator and consists of 3×3 convolutions followed by a rectified linear unit (ReLU) and batch normalization. The yellow arrows between the separate blocks at each stage are not shown for simplicity. A red arrow is a 2×2 average pooling operator and reduces the size of the layers by four. In addition, a blue arrow is 2×2 average unpooling operator, reducing the number of channels by half and increasing the size of the layer by four. A violet arrow is the skip and concatenation operator. A green arrow is the simple 1×1 convolution operator generating final reconstruction image. The total number of trainable parameters is about 22,000,000.

As for comparison, we implemented two additional algorithms: a deep convolutional neural network using FDK reconstruction (FDK-CNN), and TV penalized MBIR algorithm. The FDK-CNN was trained to learn the artifact-free images

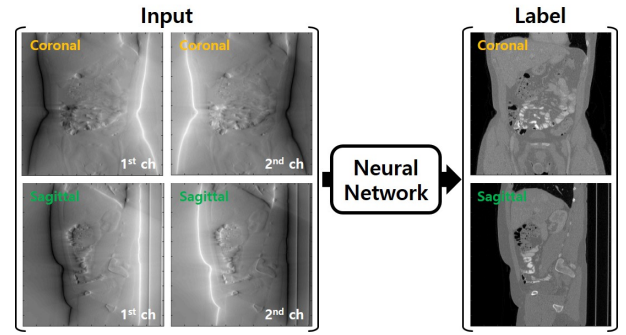


Fig. 7: Proposed network input/output for conebeam artifact removal.

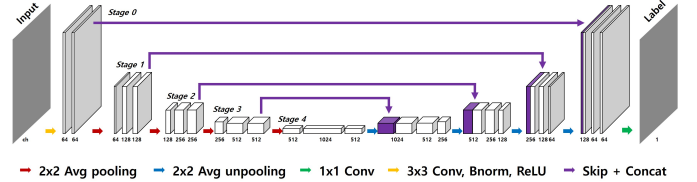


Fig. 8: U-Net backbone for our method and FDK-CNN.

from the reconstructed images of the FDK algorithm using the incomplete projection data due to the cone angle. The input image is FDK images corrupted with the cone-beam artifact,

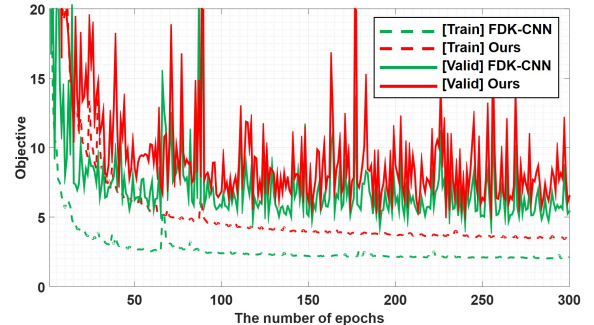


Fig. 9: Convergence plots for the objective function. [Train] : training curve. [Valid] : validation curve.

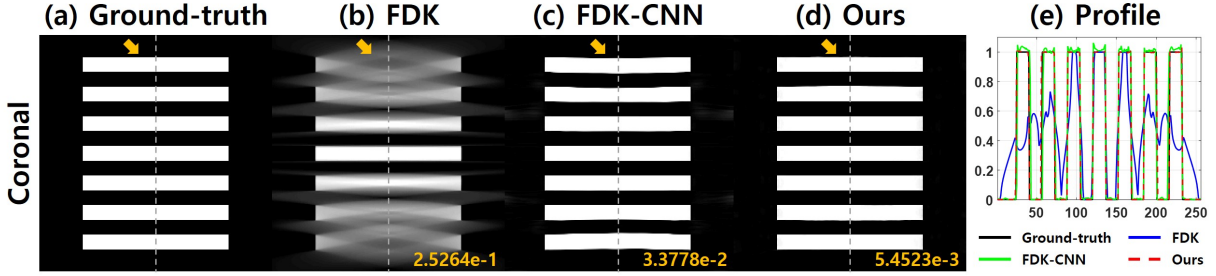


Fig. 10: Disk phantom reconstruction results from (c) FDK-CNN, and (d) proposed method. (e) shows the profiles along the gray line of the images. The number written to the images is the NMSE value.

whereas the artifact-free data is used as the ground truth. For a fair comparison, the coronal and sagittal views images are used as the network input similar to our DBP domain network. Note that FDK reconstruction combines projections from all full scan angle, so we cannot obtain the two different FDK images for each processing direction. This is why only two images along coronal and sagittal views are provided as inputs. The same U-Net architecture was also used for FDK domain neural networks. Accordingly, only difference from the proposed DBP domain deep network is the input images.

The total variation (TV) penalized reconstruction is also implemented by solving the following optimization problem:

$$\min_x \frac{1}{2} \|\mathbf{y} - \mathbf{A}\mathbf{f}\|_2^2 + \lambda (|\nabla_x \mathbf{f}|_1 + |\nabla_y \mathbf{f}|_1 + |\nabla_z \mathbf{f}|_1),$$

where \mathbf{y} and \mathbf{f} are measured sinogram data and its 3-D image, \mathbf{A} denotes a system matrix, $\nabla_{x,y,z}$ denotes differentiated operator along (x, y, z) -axes, and λ is a regularization factor.

For quantitative evaluation, the normalized mean square error (NMSE) value was used, which is defined as

$$\text{NMSE} = \frac{\sum_{i=1}^M \sum_{j=1}^N [f^*(i, j) - x(i, j)]^2}{\sum_{i=1}^M \sum_{j=1}^N [f^*(i, j)]^2}, \quad (12)$$

where f and f^* denote the reconstructed images and ground truth, respectively. M and N are the number of pixel for row and column. We also use the peak signal to noise ratio (PSNR), which is defined by

$$\text{PSNR} = 20 \cdot \log_{10} \left(\frac{NM \|f^*\|_{\infty}}{\|f - f^*\|_2} \right). \quad (13)$$

We also use the structural similarity (SSIM) index [31], defined as

$$\text{SSIM} = \frac{(2\mu_f \mu_{f^*} + c_1)(2\sigma_{ff^*} + c_2)}{(\mu_f^2 + \mu_{f^*}^2 + c_1)(\sigma_f^2 + \sigma_{f^*}^2 + c_2)}, \quad (14)$$

where μ_f is an average of f , σ_f^2 is a variance of f and σ_{ff^*} is a covariance of f and f^* . There are two variables to stabilize the division such as $c_1 = (k_1 L)^2$ and $c_2 = (k_2 L)^2$. L is a dynamic range of the pixel intensities. k_1 and k_2 are constants by default $k_1 = 0.01$ and $k_2 = 0.03$.

C. Network Training

MatConvNet toolbox (ver.24) [32] was used to implement FDK and DBP domain networks in MATLAB R2015a environment. Processing units used in this research are Intel Core

i7-7700 (3.60 GHz) central processing unit (CPU) and GTX 1080 Ti graphics processing unit (GPU). The l_2 loss was used as the objective function of the training, and the number of epochs for training networks were 300. Stochastic gradient descent (SGD) method was used as an optimizer to train the network. The initial learning rate was 10^{-4} , which gradually dropped to 10^{-5} at each epoch. The regularization parameter was 10^{-4} . For data augmentation, the whole data set were performed with horizontal and vertical flipping. The mini-batch was used as 4 and the size of input patch is 256×256 . Since convolution operations are spatially invariant, the trained filters were used for the entire input data at the inferential phase. Training time was about 4 days. Fig. 9 shows the convergence plot for each network. The dashed and solid lines represent the objective function of the training and validation phases, respectively. Since the training and validation curves converge closely, we concluded that the networks are well-trained and not over-fitted.

Since the numerical phantoms are different from the AAPM data set, the FDK-CNN and our networks were fine-tuned using a subset of disk phantoms for evaluate the reconstruction performance of other disk phantoms. Specifically, the disk phantoms using the parameters in (a)(b)(c) of Table I was used for fine-tuning, and a disk phantom of Table I(d) is used in test phase.

V. EXPERIMENTAL RESULTS

A. Numerical phantom results

First, the reconstruction results using numerical phantom is illustrated in Fig 10. In the FDK reconstruction result in Fig 10(b), severe cone-beam artifacts were observed especially in the regions far from the mid-plane. FDK-CNN reconstruction results in Fig 10(c) can significantly improve the reconstruction quality, but the shape of the disc gradually bends as it moves away from the midplane. However, our reconstruction method provided near perfect reconstruction without any bending artifacts as observed in Fig 10(d). Quantitative NMSE value on each figure clearly confirmed that the proposed method significantly outperform other methods.

B. AAPM data results

Fig. 11 shows the reconstruction images of AAPM data along the coronal and sagittal planes. As shown in Fig. 11, the FDK reconstructions around the midplane are similar to

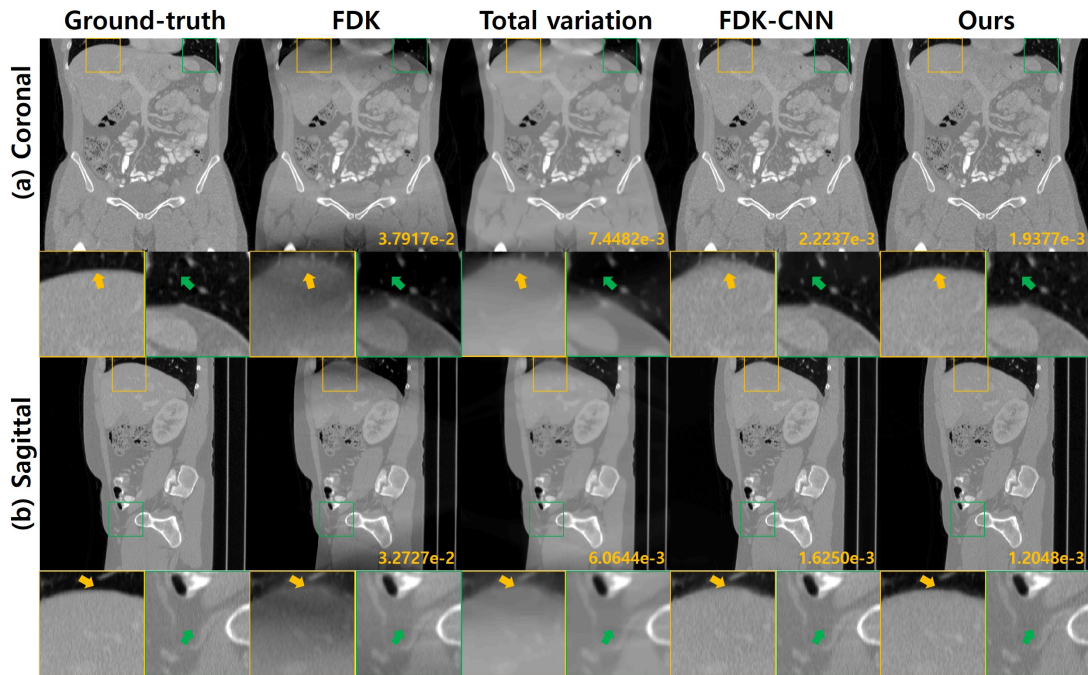


Fig. 11: (a) Coronal and (b) sagittal reconstruction results from cone-beam geometry. Yellow and green boxes illustrate the enlarged views of different parts. The number written to the images is the NMSE value.

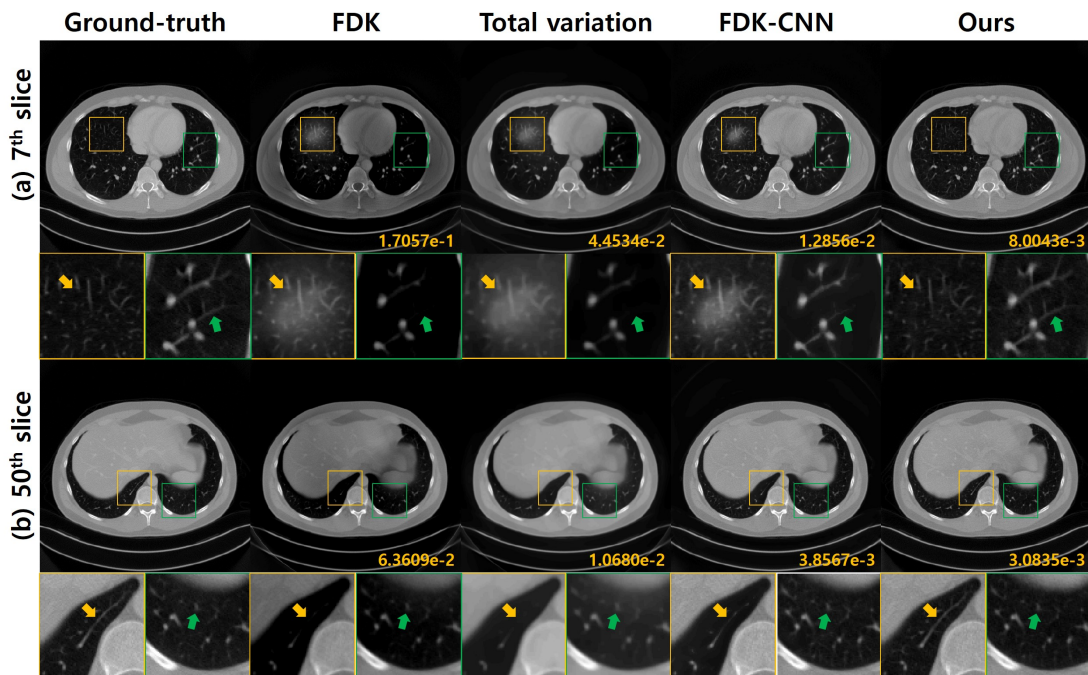


Fig. 12: Reconstruction results from Total variation, FDK-CNN, and proposed method. Yellow and green boxes illustrate the enlarged views of different parts. The number written to the images is the NMSE value.

the ground-truth images, but poor intensity and the cone-beam artifact are visible in the off-midplanes such as top and bottom areas. Although TV and FDK-CNN methods can improve the image quality, there are still remaining conebeam artifacts, and the reconstruction do not preserve the detailed structures and textures. On the other hand, our method clearly removes the artifact, maintains sophisticated structures and textures.

Table II shows the quantitative comparisons of average PSNR, NSME, and SSIM and their computation times. Our method produces the best quantitative values in all metrics. The computation time of the our network is slightly slower than that of FDK-CNN because the input size of our method is twice that of the FDK-CNN, but the neural network methods are 100 times faster than MBIR method.

Fig. 12 shows the axial view of the reconstruction results. The FDK image shows poor intensity and produces cone-beam artifacts due to the higher cone angles. While the TV and FDK-CNN methods compensate for the poor intensity, the cone-beam artifact still remained. In addition, the TV method does not preserve the detail texture, and the FDK-CNN overestimates in Fig. 12(a) or underestimates in Fig. 12(b). However, the ours method preserved the detailed texture and clearly removed the cone-beam artifacts as shown in the enlarged images of Fig. 12.

Metric	FDK	Total variation	FDK-CNN	Ours
PSNR [dB]	28.6372	33.3895	37.6277	38.4254
NMSE ($\times 10^{-3}$)	38.843	8.3376	2.7188	2.0648
SSIM	0.7767	0.7750	0.8143	0.9550
Time [sec/slice]	-	14.06	0.10	0.12

TABLE II: Quantitative comparison for various algorithms.

To demonstrate the importance of spectral blending, the reconstruction results by separate processing along the coronal and the sagittal direction are shown in Fig. 13(c)(d), whereas the results from the spectral blending is shown in Fig. 13(e). The horizontal and vertical streaking artifacts patterns are visible in the axial view images in Fig. 13(c)(d), respectively, where the artifact patterns appears along the direction of plane of interests. On the other hand, the spectral blending removes the streaking patterns as shown in Fig. 13(e). In the coronal and sagittal view reconstruction results, the results without the spectral blending exhibited remaining streaking patterns, whereas our method with spectral blending has successfully removed them. The PSNR values in Table III also confirmed that the spectral blending improves the reconstruction quality.

	(i) Ours sagittal	(ii) Ours coronal	(iii) Ours
PSNR [dB]	37.6270	36.2836	38.4254

TABLE III: Quantitative comparison to validate the importance of spectral blending.

VI. CONCLUSIONS

In this paper, we developed a novel DBP domain deep learning approach for conebeam artifacts removal. Inspired by the existing factorization approach that converts 3-D problem into a successive 2-D deconvolution along the plane of interest, our neural network is designed as a 2-D neural network for each plane of interest and was trained to learn the mapping between DBP data and the artifact-free images. Furthermore, spectral blending technique, which mixes the spectral components of the coronal and sagittal reconstruction, was employed to mitigate the missing frequency occurred along the plane of interest direction. Experimental results showed that the our method is quantitatively and qualitatively superior to the existing methods, despite significantly reduced computational runtime.

VII. ACKNOWLEDGEMENT

The authors would like to thanks Dr. Cynthia MaCollough, the Mayo Clinic, the American Association of Physicists in

Medicine (AAPM), and grant EB01705 and EB01785 from the National Institute of Biomedical Imaging and Bioengineering for providing the Low-Dose CT Grand Challenge data set. This work is supported by National Research Foundation (NRF) of Korea, Grant number NRF2016R1A2B3008104 and Industrial Strategic technology development program (10072064, Development of Novel Artificial Intelligence Technologies To Assist Imaging Diagnosis of Pulmonary, Hepatic, and Cardiac Disease and Their Integration into Commercial Clinical PACS Platforms) funded by the Ministry of Trade Industry and Energy (MI, Korea).

APPENDIX

In our recent work [24], we showed that the output of a CNN composed of κ layer of encoder and decoder without skipped connection can be represented by the following basis-like representation:

$$f := \mathcal{T}_{\Theta}g = \sum_i \langle b_i(g), g \rangle \tilde{b}_i(g) = \tilde{B}(g)B(g)^\top g \quad (15)$$

where $b_i(g)$ and $\tilde{b}_i(g)$ denote the i -th column of the following frame basis and its dual:

$$B(g) = E^1 \Sigma^1(g) E^2 \dots \Sigma^{\kappa-1}(g) E^\kappa, \quad (16)$$

$$\tilde{B}(g) = D^1 \tilde{\Sigma}^1(g) D^2 \dots \tilde{\Sigma}^{\kappa-1}(g) D^\kappa \quad (17)$$

where E^l (resp. D^l) refers to the encoder (resp. decoder) matrices, respectively, which are determined by pooling (resp. unpooling) operation and convolution filters [24], and $\Sigma^l(g)$ and $\tilde{\Sigma}^l(g)$ denote the diagonal matrix with 0 and 1 values that are determined by the ReLU output in the previous convolution steps. For the case of encoder-decoder CNN with the skipped connection, similar basis expression can be obtained [24].

Since the ReLU nonlinearity is applied after the convolution operation, the on-and-off activation pattern of each ReLU determines a binary partition of the feature space at each layer across the hyperplane that is determined by the convolution. Accordingly, one of the most important observation in [24] is that the input space \mathcal{X} is partitioned into multiple non-overlapping regions as shown in Fig. 14 so that input images for each region share the same linear representation, but overall representation is still non-linear. This implies that two different input images in Fig. 14 are automatically switched to two distinct linear representations that are different from each other.

This input adaptivity poses an important computational advantage over the classical sparse representation learning approaches such as compressed sensing, which relies on computationally expensive l_1 minimization approaches. In addition, the number of linear representation increases exponentially with the width and depth of the neural network as well as the skipped connection. This exponentially large expressivity, synergistically combined with the aforementioned input adaptivity, can make the neural network approaches so powerful.

REFERENCES

- [1] L. A. Feldkamp, L. Davis, and J. W. Kress, "Practical cone-beam algorithm," *Josa a*, vol. 1, no. 6, pp. 612–619, 1984.

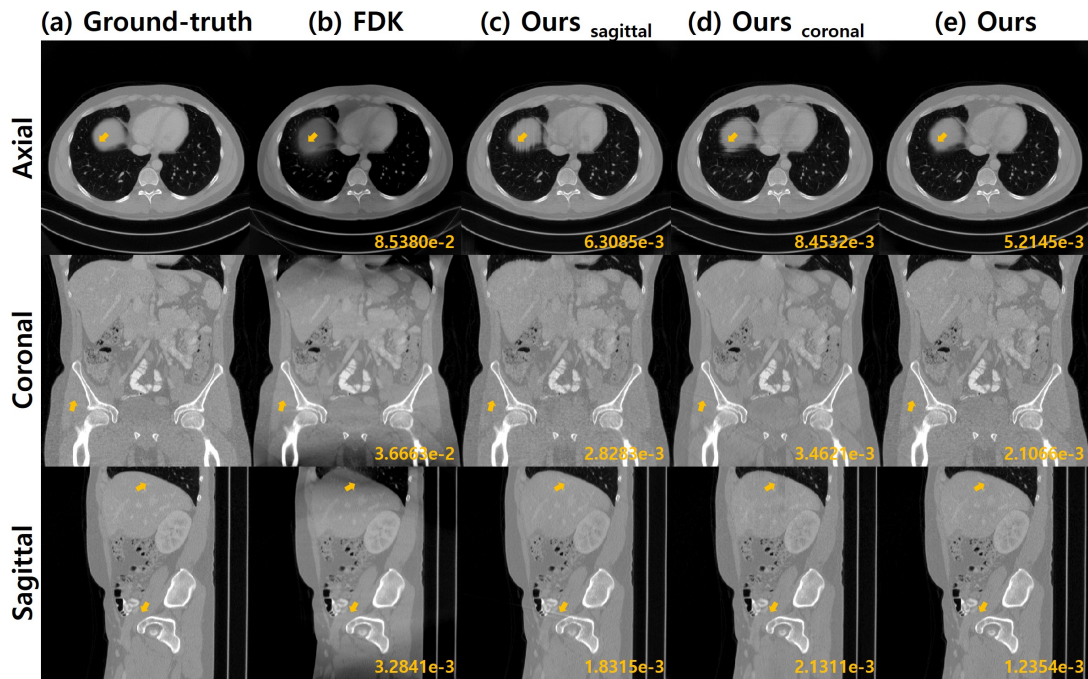


Fig. 13: Reconstruction results with and without spectral blending. The number written to the images is the NMSE value. (c) is reconstructed into a single network of sagittal DBP input, but (d) is reconstructed from coronal DBP input. (e) is reconstructed from spectral blending between (c) and (d).

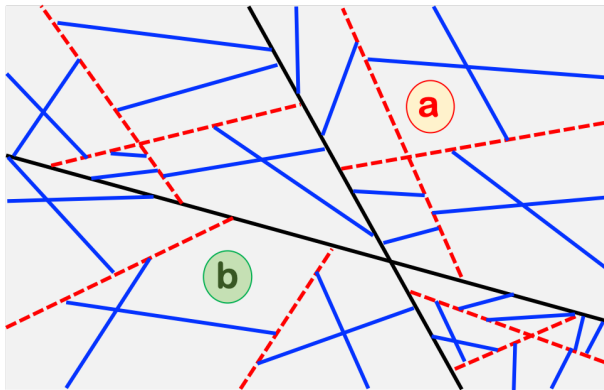


Fig. 14: High level illustration of input space partitioning concept from three layer neural networks. In this figure, the partition boundaries with black, blue and red colors are determined by the convolution filters at the first, second, and the third layer. Due to the partitioning, the input signals in (a) and (b) are automatically switched to two distinct linear representations.

- [2] M. Grass, T. Köhler, and R. Proksa, "Angular weighted hybrid cone-beam ct reconstruction for circular trajectories," *Physics in Medicine & Biology*, vol. 46, no. 6, p. 1595, 2001.
- [3] X. Tang, J. Hsieh, A. Hagiwara, R. A. Nilsen, J.-B. Thibault, and E. Drapkin, "A three-dimensional weighted cone beam filtered back-projection (CB-FBP) algorithm for image reconstruction in volumetric CT under a circular source trajectory," *Physics in Medicine & Biology*, vol. 50, no. 16, p. 3889, 2005.
- [4] S. Mori, M. Endo, S. Komatsu, S. Kandatsu, T. Yashiro, and M. Baba, "A combination-weighted feldkamp-based reconstruction algorithm for cone-beam ct," *Physics in Medicine & Biology*, vol. 51, no. 16, p. 3953, 2006.
- [5] H. K. Tuy, "An inversion formula for cone-beam reconstruction," *SIAM Journal on Applied Mathematics*, vol. 43, no. 3, pp. 546–552, 1983.
- [6] S. Bartolac, R. Clackdoyle, F. Noo, J. Siewerdsen, D. Moseley, and D. Jaffray, "A local shift-variant Fourier model and experimental validation of circular cone-beam computed tomography artifacts," *Medical Physics*, vol. 36, no. 2, pp. 500–512, 2009.
- [7] J. D. Pack, Z. Yin, K. Zeng, and B. E. Nett, "Mitigating cone-beam artifacts in short-scan CT imaging for large cone-angle scans," *Fully 3D Image Reconstruction in Radiology and Nuclear Medicine*, pp. 307–310, 2013.
- [8] F. Peyrin, M. Amiel, and R. Goutte, "Analysis of a cone beam x-ray tomographic system for different scanning modes," *Journal of the Optical Society of America A*, vol. 9, no. 9, pp. 1554–1563, 1992.
- [9] E. Y. Sidky and X. Pan, "Image reconstruction in circular cone-beam computed tomography by constrained, total-variation minimization," *Physics in Medicine & Biology*, vol. 53, no. 17, p. 4777, 2008.
- [10] E. Y. Sidky, J. H. Jørgensen, and X. Pan, "Convex optimization problem prototyping for image reconstruction in computed tomography with the chambolle-pock algorithm," *Physics in Medicine & Biology*, vol. 57, no. 10, p. 3065, 2012.
- [11] Z. Zhang, X. Han, E. Pearson, C. Pelizzari, E. Y. Sidky, and X. Pan, "Artifact reduction in short-scan cbct by use of optimization-based reconstruction," *Physics in Medicine & Biology*, vol. 61, no. 9, p. 3387, 2016.
- [12] D. Xia, D. A. Langan, S. B. Solomon, Z. Zhang, B. Chen, H. Lai, E. Y. Sidky, and X. Pan, "Optimization-based image reconstruction with artifact reduction in c-arm cbct," *Physics in Medicine & Biology*, vol. 61, no. 20, p. 7300, 2016.
- [13] A. Krizhevsky, I. Sutskever, and G. E. Hinton, "Imagenet classification with deep convolutional neural networks," in *Advances in neural information processing systems*, 2012, pp. 1097–1105.
- [14] O. Ronneberger, P. Fischer, and T. Brox, "U-net: Convolutional networks for biomedical image segmentation," in *International Conference on Medical Image Computing and Computer-Assisted Intervention - MICCAI 2015*. Springer, 2015, pp. 234–241.
- [15] Y. Han, J. Yoo, and J. C. Ye, "Deep residual learning for compressed sensing CT reconstruction via persistent homology analysis," *arXiv preprint arXiv:1611.06391*, 2016.
- [16] E. Kang, J. Min, and J. C. Ye, "A deep convolutional neural network using directional wavelets for low-dose x-ray ct reconstruction," *Medical physics*, vol. 44, no. 10, 2017.
- [17] H. Chen, Y. Zhang, M. K. Kalra, F. Lin, Y. Chen, P. Liao, J. Zhou, and G. Wang, "Low-dose ct with a residual encoder-decoder convolutional

- neural network,” *IEEE transactions on medical imaging*, vol. 36, no. 12, pp. 2524–2535, 2017.
- [18] K. H. Jin, M. T. McCann, E. Froustey, and M. Unser, “Deep convolutional neural network for inverse problems in imaging,” *IEEE Transactions on Image Processing*, vol. 26, no. 9, pp. 4509–4522, 2017.
- [19] E. Kang, W. Chang, J. Yoo, and J. C. Ye, “Deep convolutional framelet denoising for low-dose CT via wavelet residual network,” *IEEE Transactions on Medical Imaging*, vol. 37, no. 6, pp. 1358–1369, 2018.
- [20] Y. Han and J. C. Ye, “Framing U-Net via deep convolutional framelets: Application to sparse-view CT,” *IEEE Transactions on Medical Imaging*, vol. 37, no. 6, pp. 1418–1429, 2018.
- [21] Y. Han, J. Gu, and J. C. Ye, “Deep learning interior tomography for region-of-interest reconstruction,” in *Proceedings of The Fifth International Conference on Image Formation in X-Ray Computed Tomography*, 2018.
- [22] Y. Han and J. C. Ye, “One network to solve all ROIs: Deep learning ct for any ROI using differentiated backprojection,” *Medical Physics (in press)*, Also available as *arXiv preprint arXiv:1810.00500*, 2018.
- [23] J. C. Ye, Y. Han, and E. Cha, “Deep convolutional framelets: A general deep learning framework for inverse problems,” *SIAM Journal on Imaging Sciences*, vol. 11, no. 2, pp. 991–1048, 2018.
- [24] J. C. Ye and W. K. Sung, “Understanding geometry of encoder-decoder CNNs,” in *Proceedings of the 36th International Conference on Machine Learning*, ser. Proceedings of Machine Learning Research, K. Chaudhuri and R. Salakhutdinov, Eds., vol. 97. Long Beach, California, USA: PMLR, 09–15 Jun 2019, pp. 7064–7073.
- [25] M. Lee, Y. Han, J. P. Ward, M. Unser, and J. C. Ye, “Interior tomography using 1d generalized total variation. part ii: Multiscale implementation,” *SIAM Journal on Imaging Sciences*, vol. 8, no. 4, pp. 2452–2486, 2015.
- [26] F. Dennerlein, F. Noo, H. Schondube, G. Lauritsch, and J. Hornegger, “A factorization approach for cone-beam reconstruction on a circular short-scan,” *IEEE Transactions on Medical Imaging*, vol. 27, no. 7, pp. 887–896, 2008.
- [27] J. D. Pack and F. Noo, “Cone-beam reconstruction using 1D filtering along the projection of M-lines,” *Inverse Problems*, vol. 21, no. 3, p. 1105, 2005.
- [28] Y. Zou and X. Pan, “Exact image reconstruction on PI-lines from minimum data in helical cone-beam CT,” *Physics in Medicine and Biology*, vol. 49, no. 6, p. 941, 2004.
- [29] —, “Image reconstruction on pi-lines by use of filtered backprojection in helical cone-beam ct,” *Physics in Medicine & Biology*, vol. 49, no. 12, p. 2717, 2004.
- [30] L. Yu, Y. Zou, E. Y. Sidky, C. A. Pelizzari, P. Munro, and X. Pan, “Region of interest reconstruction from truncated data in circular cone-beam ct,” *IEEE transactions on medical imaging*, vol. 25, no. 7, pp. 869–881, 2006.
- [31] Z. Wang, A. C. Bovik, H. R. Sheikh, and E. P. Simoncelli, “Image quality assessment: from error visibility to structural similarity,” *IEEE transactions on image processing*, vol. 13, no. 4, pp. 600–612, 2004.
- [32] A. Vedaldi and K. Lenc, “MatConvNet: Convolutional neural networks for MATLAB,” in *Proceedings of the 23rd ACM International Conference on Multimedia*. ACM, 2015, pp. 689–692.